



 Cite this: *RSC Adv.*, 2023, **13**, 2672

# High-performance SiGe anode materials obtained by dealloying a Sr-modified Al–Si–Ge eutectic precursor†

 Huajie Zhang and Jinfu Li \*

In exploring the anode materials for high efficiency Li-ion batteries, it has been found that the electrochemical performance of Si can be enhanced *via* alloying with Ge. In the present work, we modified the Al–Si–Ge eutectic ribbons as the precursor by adding a trace of Sr to the alloy. The SiGe particles obtained by dealloying the Al–Si–Ge eutectic precursor have a porous coral-like nano-architecture with numerous fibrous branches towards various directions. Because of the large surface area and porosity, the as-prepared Sr-modified SiGe anode delivers an excellent capacity of 1166.6 mA h g<sup>-1</sup> at 0.1 A g<sup>-1</sup> after 100 cycles with a fantastic initial coulombic efficiency of 83.62%. Besides, it has a superior rate performance with a reversible capacity of 675.3 mA h g<sup>-1</sup> at the current density of 8 A g<sup>-1</sup>. It is demonstrated that the modification treatment that is widely used in metallurgy is also a promising strategy to synthesize high-performance battery electrodes and other energy storage materials.

Received 2nd December 2022

Accepted 6th January 2023

DOI: 10.1039/d2ra07674h

[rsc.li/rsc-advances](https://rsc.li/rsc-advances)

## Introduction

At present Li-ion batteries (LIBs) have been extensively used in the fields of vehicles, portable electronic equipment, energy storage and so on,<sup>1,2</sup> and are facing growing demands for longer cycling life and higher rate capacity. As a promising anode material for next generation LIBs, silicon (Si) has a theoretical capacity up to 3579 mA h g<sup>-1</sup>, and abundant availability as well as low discharge potential of about 0.2 V.<sup>3,4</sup> However, it is also confronted with a low initial coulombic efficiency and poor reversibility due to the large volume change during the charge/discharge process,<sup>3,5</sup> intrinsic low electron conductivity<sup>6</sup> and slow kinetics of lithium transportation.<sup>7</sup> Owing to the iso-valence and iso-morphism, Ge demonstrates the potential to optimize the performance of Si anodes, as one of the most promising alloying strategies. The addition of Ge can contribute to the transport of lithium and boost the rate capability since Ge dopant atoms expand the lattice and reduce the energy barrier of Li-ion diffusion, therefore minimizing Li-ion trapping.<sup>8,9</sup> Also, the lithiation/de-lithiation of Si and Ge occurs at different onset potentials, meaning the non-simultaneous volume expansion, which benefits the gradual release of strain-stress.<sup>10,11</sup>

In addition to alloying strategy, different methods have also been explored to synthesize nanoscale Si(Ge)-based anodes with diverse structures, in order to overcome the aforementioned disadvantages,<sup>12–14</sup> such as chemical reduction for 0D particles,<sup>15</sup> metal-assisted solution etching or electro-deposition for nanoarrays,<sup>16,17</sup> sputter deposition for films,<sup>18,19</sup> *etc.* Most of them are multistep synthesis with poor productivity and usually cost expensive templates, hindering the large-scale application in the manufacture. In recent years, dealloying has been proven to be an effective and facile method to fabricate self-supported 3D nanoporous materials including Si anodes.<sup>20–23</sup> Yang *et al.*<sup>8</sup> dealloyed as-prepared ternary Al–Si–Ge ribbons, and successfully prepared the 3D-NP coral-like Si (Ge) particles with a high reversible capacity of 1158 mA h g<sup>-1</sup> after 150 cycles at a current density of 100 mA g<sup>-1</sup> besides the excellent rate capacity. Sohn and his co-workers<sup>24</sup> etched the melt-spun Si/Al–Cu–Fe composite using acidic and alkaline solutions sequentially, and obtained a high-performance 3D porous Si anode material, while still maintaining capacities as high as 1222 mA h g<sup>-1</sup> even after 200 cycles. Therefore, dealloying is promising to be a scalable, cost-effective way to fabricate porous Si anode materials suitable for high energy density commercial LIBs.

Modification is a common approach in industry to introduce structural transformation by adding minor elements, and is expected to be applied in the nanoarchitecture design of Si anodes. The chemical elements used to modify Al–Si(Ge) alloys include Na, P, Sr, Ce as well as some rare earth metals.<sup>25,26</sup> Generally, eutectic Si(Ge) is presented in the form of elongated plates in unmodified Al–Si(Ge) alloys, but will be transformed into a fine fibrous structure in the modified alloys.<sup>27,28</sup> If Al–

State Key Laboratory of Metal Matrix Composites, School of Materials Science and Engineering, Shanghai Jiao Tong University, Shanghai 200240, China. E-mail: jfli@sjtu.edu.cn; Fax: +86 21 54748530

† Electronic supplementary information (ESI) available. See DOI: <https://doi.org/10.1039/d2ra07674h>



Si(Ge) alloys are solidified at high cooling rates, for example by melt spinning, the solid solubility of Si(Ge) in  $\alpha$ -Al will be extended while the Si(Ge) phase is refined.<sup>29,30</sup> During the subsequent dealloying, the Si and Ge dissolved in  $\alpha$ -Al phase tend to re-assemble onto the exposed eutectic Si(Ge) phase, changing the morphology of Si(Ge). Jiang and Li<sup>28</sup> prepared the Sr-modified porous silicon by dealloying the melt-spun Al–Si ribbons, which delivers a stable capacity of 594.8 mA h g<sup>-1</sup> at a high current density of 2 A g<sup>-1</sup> after 50 cycles. However, it is unclear how the modification elements influence the final structures during the dealloying process, and the performance is limited by the intrinsic feature of used system. Therefore, it is attractive to explore the element modification in more potential systems and study the dealloying process in depth.

Herein, we prepared 3D nanoporous SiGe particles by dealloying the eutectic Al–Si–Ge ribbons modified by a trace of Sr. Then half-coin cells were assembled to measure the electrochemical performance, applying the as-prepared SiGe particles as active materials for anodes. It was verified that the addition of Sr contributes to good cycling performance and rate capability by refining the eutectic SiGe phases. This strategy to apply the chemical modification in metallurgy into the synthesis of SiGe anodes makes it possible to improve the performance of LIB electrodes and other energy storage materials.

## Experimental

It has been reported that the SiGe anode with a ratio of Si/(Si + Ge) at 0.5–0.7 showed better electrochemical performance in both cycle stability and rate capability.<sup>8,17,19</sup> Concerning the intrinsic finer structure of the eutectic alloy, we prepared the precursor of Al<sub>84.23</sub>Si<sub>9.46</sub>Ge<sub>6.31</sub> (atomic percentage) eutectic composition with the median Si/(Si + Ge) value at 0.6, according to the experimental phase diagrams.<sup>31–34</sup> The nominal doping content of Sr in this work is 0.04 wt%, which has been proved to be enough to modify the eutectic Si phase in Al–Si alloys.<sup>26–28</sup>

The Al<sub>84.23</sub>Si<sub>9.46</sub>Ge<sub>6.31</sub> alloy ingots were prepared by melting the mixture of pure Al (99.999%), pure Si (99.999%), pure Ge (99.999%) and Al–10Sr (wt%) master alloy in an arc melting furnace filled with high-purity argon. The alloy ingots were then heated to 1100 °C rapidly, and the melt was ejected onto a rotating copper wheel at a circumferential speed of  $\sim 35$  m s<sup>-1</sup> in a single roller melt-spinning apparatus. Ribbons of  $\sim 5$  mm wide, 40–60  $\mu$ m thick and several meters long were obtained. The dealloying process was conducted in a 5 wt% HCl aqueous solution water-bathed at 60 °C with vigorous magnetic stirring at the rate of 600 rpm for more than 24 h, until there were no more bubbles to escape from the solution. The as-dealloyed samples were washed and dried, and then kept in a vacuum glove box to avoid oxidation.

The phase constitution was characterized by an X-ray diffractometer (XRD, D8 ADVANCE Da Vinci), with Cu K $\alpha$  radiation at 40 kV and scanning angle ( $2\theta$ ) ranging from 20° to 90° at a scan rate of 4° min<sup>-1</sup>. The XRD results were also used to judge whether the Al sacrificed completely. The microstructure and composition were characterized by an optical microscope (OM), and a scanning electron microscope (SEM, RISE-MAGNA,

TESCAN) equipped with energy dispersive X-ray spectroscopy (EDS) detector. Particle size was measured in a laser particle sizer (S3500). The nitrogen adsorption–desorption measurement was conducted in a specific surface area and porosity analyzer (Autosorb-IQ3) at 25 °C. Barrett–Joyner–Halenda (BJH) and Brunauer–Emmett–Teller (BET) methods were adopted to calculate the pore volume, pore distribution as well as surface area.

2025 half-coin cells were assembled to measure the electrochemical performance. Slurries for working electrode were prepared by mixing the active materials, acetylene black and carboxyl methyl cellulose (CMC) at a mass ratio of 7 : 2 : 1. Then the slurries were coated with a thickness of 50  $\mu$ m on a Cu foil current collector and dried in a vacuum at 80 °C for 12 h. The mass loading of active materials (SiGe) is in the range of 0.5–0.6 mg cm<sup>-2</sup>. Then the half-coin cells were assembled in an argon-filled glove box at room temperature with a Li foil as the counter electrode, a polypropylene film (Celgard-2400) as the separator, and the used electrolyte is 1 M LiPF<sub>6</sub> solution in a mixture of ethylene carbonate/dimethyl carbonate/methyl ethyl carbonate (EC/DEC/EMC, 1 : 1 : 1 vol%) with 1.0% vinylene carbonate (VC). Galvanostatic discharge/charge cycles were carried out in a battery cyler (LAND, Wuhan, China) at a current density of 1000 mA g<sup>-1</sup> with a voltage between 0.01 and 1 V. Before the measurement of the rate capacity, the anode materials were activated at a current density of 100 mA g<sup>-1</sup>. The cyclic voltammetry (CV) measurements were performed at a sweep rate of 0.1 mV s<sup>-1</sup> from 0.01 to 1.5 V (vs. Li/Li<sup>+</sup>) on the electrochemical workstation (CHI 760E, Shanghai, China). Electrochemical impedance spectroscopy (EIS) measurements were performed with a frequency range of 0.01 Hz to 100 kHz.

## Results and discussion

### Structure of Al–Si–Ge precursor and dealloying process

As shown in Fig. 1, the fully solidified Al–Si–Ge precursors are composed of primary  $\alpha$ -Al phase and the eutectic  $\alpha$ -Al/SiGe phase. According to the EDS mapping results provided in the ESI† (Fig. S1†), the primary  $\alpha$ -Al phase grew into dendrites

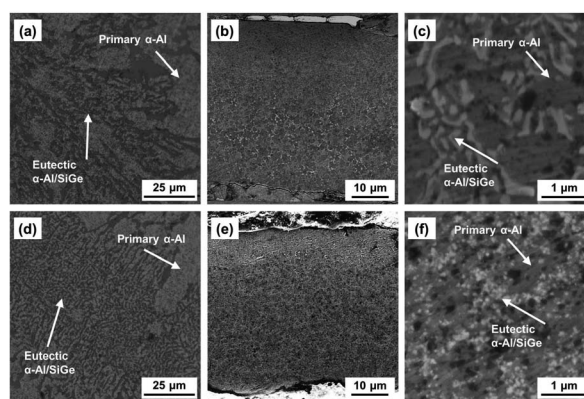


Fig. 1 SEM images of the microstructure of Al<sub>84.23</sub>Si<sub>9.46</sub>Ge<sub>6.31</sub> eutectic alloy: unmodified (a) alloy ingot and (b and c) ribbon; Sr-modified (d) alloy ingot and (e and f) ribbon.



around which is the  $\alpha$ -Al/SiGe eutectic. Because the rapidly solidified  $\alpha$ -Al phase dissolves more Si and Ge atoms than the equilibrium solidification under the ultra-high cooling rate, the obtained sample is off the complete eutectic structure. Compared with the phase distribution in the unmodified ingot shown in Fig. 1(a), the addition of Sr realizes the “flake to fibrous” morphological transformation, resulting in more uniform phase distribution (Fig. 1(d)). Similarly, the microstructures of the spinning-melt ribbons verify the refinement effect of Sr in addition to the fast-cooling method. In unmodified ribbons of Fig. 1(b) and (c), SiGe crystals present thick plate structures with irregular distribution, typically looking like coarse needles or strips. Fig. 1(e) and (f) shows that the Sr-modified SiGe eutectic phase appears as finer and denser dots on the cross section. This transformation can be explained by the twin-plane reentrant edge mechanism (TPRE) and impurity-induced twinning mechanism (IIT).<sup>27,35–38</sup> Previous studies have revealed that Sr atoms are mainly distributed relatively uniformly in the eutectic SiGe phase while the dissolution in primary and eutectic Al phase is negligible.<sup>25,26</sup> During solidification, Sr atoms prefer to locate on the growth steps of the SiGe solid–liquid interface and create new twin plane reentrant edges. As a result, Sr transforms the thick and large-scale growth model of coarse branches into a small fibrous growth model with a large number of frequent branches.

Immersed in a 5 wt% aqueous HCl for enough time, the  $\alpha$ -Al phase reacted with the acid and the previous ribbons were converted into particles. The XRD patterns of the products after different reaction time are shown in Fig. 2(a). The initial ribbons consists of  $\alpha$ -Al phase and SiGe phase. With the dealloying proceeding, Al was sacrificed but SiGe remained. There is little difference in the XRD patterns of the unmodified and Sr-modified particles as shown in Fig. 2(b). The amount of Sr is so minor that its influence on the phase structure is difficult to be detected by the X-ray response.

### Morphology and porosity of 3D nanoporous SiGe particles

Fig. 3(a) and (b) shows the typical morphology of unmodified and Sr-modified particles. Both particles have 3D porous structures composed of numerous branches that can provide enough active surface area for the electrochemical process. The particles basically maintain the microstructure in the ribbon to a certain degree, *i.e.*, the unmodified particle consists of plate branches while the modified one of fibrous branches which

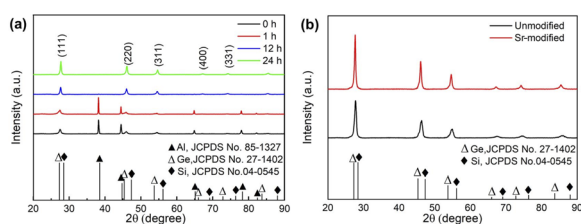


Fig. 2 XRD patterns of (a) the Sr-modified  $\text{Al}_{84.23}\text{Si}_{9.46}\text{Ge}_{6.31}$  ribbons dealloyed in 5 wt% HCl aqueous solution for different time and (b) the completely dealloyed products of  $\text{Al}_{84.23}\text{Si}_{9.46}\text{Ge}_{6.31}$  ribbons.

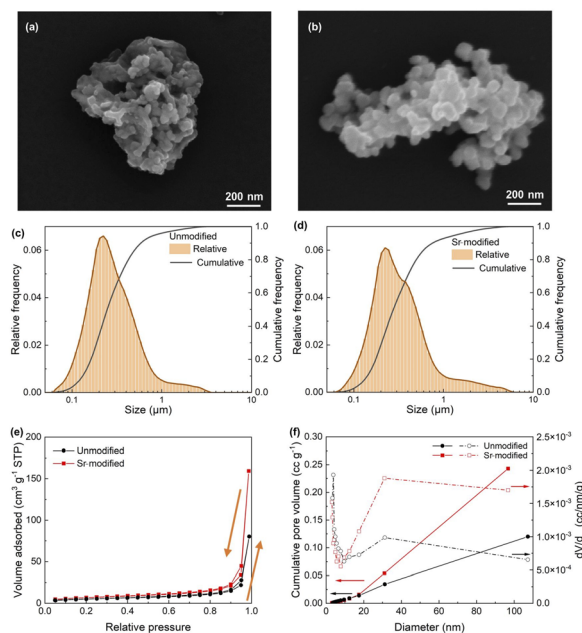


Fig. 3 Detailed information of SiGe particles obtained by dealloying the unmodified and Sr-modified  $\text{Al}_{84.23}\text{Si}_{9.46}\text{Ge}_{6.31}$  ribbons: (a and b) SEM images, (c and d) size distributions, (e)  $\text{N}_2$  adsorption–desorption isotherms and (f) corresponding pore size distributions calculated by the BJH method.

provides the particle with more three-dimensional nano-architecture. Therefore, the modified particles have increasing surface and more sufficient space for Li-ion to insert/desert during the charging/discharging process. As shown in Fig. 3(c) and (d), the two types of particles are close to the normal distribution, ranging from 100 nm to 1  $\mu\text{m}$ . The detailed information is listed in Table 1. The  $D_{50}$  of unmodified and Sr-modified particles is 246 nm and 276 nm, respectively. The particle size is closely related with the eutectic colonies in the ribbon. Thus, it is clear that the modification did not change the size of the eutectic colonies significantly.

The specific surface area and pore size distribution of as-prepared SiGe particles were measured in the  $\text{N}_2$  adsorption and desorption method, and the isotherms are presented in Fig. 3(e). They can be identified as the type IV adsorption isotherms with an H3-type hysteresis loop according to the International Union of Pure and Applied Chemistry (IUPAC) classification. It suggests that capillary condensation takes place at higher pressures of adsorbate in addition to multilayer adsorption at lower pressures, indicating the existence of mesopores and micropores in the as-prepared powders.<sup>8,39,40</sup> Besides, Fig. 3(f) verifies the coexistence of micropores and

Table 1 Detailed information for particle analysis

Sample	$D_{50}$ (nm)	Surface area ( $\text{m}^2 \text{g}^{-1}$ )	Pore volume ( $\text{cc g}^{-1}$ )	Pore diameter (nm)
Unmodified	246	12.570	0.120	3.826
Sr-modified	276	19.662	0.243	30.018



mesopores in the samples with a similar distribution. However, the addition of Sr results in the increasing adsorption amounts, which illustrates that modified SiGe particles have the larger porosity. Based on the  $N_2$  adsorption profile, Table 1 also lists the pore volume and diameter, as well as the surface area calculated by the Brunauer–Emmett–Teller (BET) method. Obviously, the modified SiGe particles have a specific surface area of  $19.662 \text{ m}^2 \text{ g}^{-1}$  while that of unmodified sample is  $12.570 \text{ m}^2 \text{ g}^{-1}$ . The larger surface area provides more electrode/electrolyte contacts and can facilitate the electrochemical reaction during the charge/discharge process. The pore volume doubled from  $0.120 \text{ cc g}^{-1}$  to  $0.243 \text{ cc g}^{-1}$  when adding trace of Sr to modify the SiGe particles. Also, the average diameter of pores shows a significant difference. The unmodified particles have a mean diameter of 3.826 nm while that for the modified ones is 31.018 nm. The shift from micropores to mesopores offers more free space to partially accommodate the lithiation-induced strain. Therefore, the Sr-modified SiGe particles have larger surface areas and porosity.

### Electrochemical performance for assembled batteries

The lithium storage performance of as-prepared samples is characterized by electrochemical impedance spectroscopy (EIS), cyclic voltammetry (CV) as well as galvanostatic charge–discharge tests. Fig. 4(a) and (b) shows the similar initial three cycle CV curves for the anodes of unmodified and modified SiGe particles as active substances in the potential window of 0.01–1.5 V (vs.  $\text{Li}/\text{Li}^+$ ) with a scan rate of  $0.1 \text{ mV s}^{-1}$ . In the cathodic scans, the peaks beginning at about 0.4 V can be ascribed to the lithiation reactions of Ge and Si,<sup>41</sup> while in the anodic scans, the shoulders at 0.2 V and the sharp peaks at  $\sim 0.6$  V can be related to the de-lithiation reactions of  $\text{Li}_x\text{Si}$  and  $\text{Li}_x\text{Ge}$ , which is reversible during the charge/discharge process.<sup>10,11</sup> Note that in the first cathodic scan, there is a more obvious broad shoulder located between 0.8 and 0.4 V for the unmodified SiGe anode,

compared to the modified one. It disappears in the following cycles, corresponding to the decomposition of electrolyte and the irreversible formation of the solid/electrolyte interphase (SEI) on the surface of the electrode.

The EIS measurements were conducted on as-prepared uncycled electrodes, and the results are displayed in Fig. 4(c) and (d). Both spectra exhibit a depressed semicircle in the high-to-medium-frequency range and a straight line in the low-frequency range. This type of spectra can usually be fitted by the inserted equivalent circuit diagram, in which  $R_s$  represents the ohmic resistance in the battery determined by the distance between two electrodes. More importantly, the high-frequency semicircle corresponds to the charge-transfer resistance ( $R_{ct}$ ), and the double-layer capacitance at the electrode/electrolyte interface (CPE), controlled by the kinetics. The inclined straight line is dominated by the mass transfer resistance of lithium-ion diffusion ( $W_o$ ).<sup>8,42</sup> As for the uncycled ones, the  $R_{ct}$  of the modified electrode is about  $79.8 \Omega$  while that of the unmodified electrode is about  $97.0 \Omega$ , verifying that the addition of Sr influences the formation of SEI and the Li alloying reaction, as listed in Table 2. For the electrodes after 5 cycles, the  $R_{ct}$  value of the unmodified one increases to about  $100.0 \Omega$ , while that for Sr-modified one drops to  $68.4 \Omega$ . That is to say, the Sr-modified SiGe anode has a relatively small ion exchange resistance during the lithium/de-lithium cycling, contributing to the reversible electrode reaction. Comparing the results before and after cycling, the slope of the inclined line segment is obviously smaller after the cycling, meaning a decreasing Warburg impedance. This is because the SiGe material is activated by several cycles under low current density, and the SEI film on the surface is stable, which reduces the interfacial layer impedance.

Fig. 5(a) compares the discharge capacities *versus* cycle numbers for as-prepared electrodes at a constant current density of  $0.1 \text{ A g}^{-1}$  between 0.01 and 1 V. After 100 cycles, the unmodified anode delivers a capacity of  $780.8 \text{ mA h g}^{-1}$  while the modified one still remains  $1166.6 \text{ mA h g}^{-1}$ . Obviously, the addition of Sr can delay the electrode degradation and prolongs the service life, because of the resultant larger surface area and porosity in the electrode. Fig. 5(b) exhibits the 1st, 2nd, 10th, 50th, and 100th cycle charge–discharge voltage profiles of the as-prepared samples. In the first cycle of the unmodified sample, the discharge and charge capacities are  $2147.7$  and  $1634.0 \text{ mA h g}^{-1}$ , respectively, with an initial coulombic efficiency (ICE) of 76.08%, but those of the Sr-modified sample are  $2842.5$  and  $2377.0 \text{ mA h g}^{-1}$ , and the ICE = 83.62%. Not only the initial coulombic efficiency but also the first cycle capacity performance are improved significantly by adding Sr, because

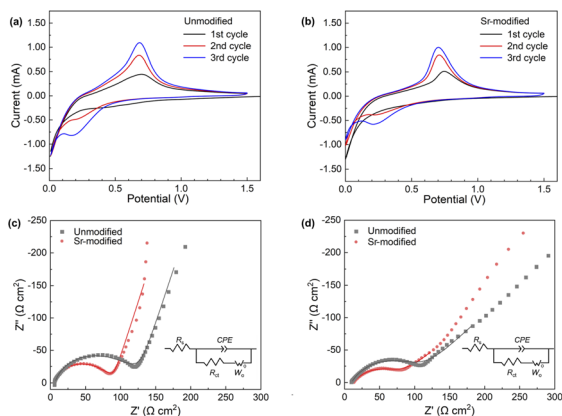


Fig. 4 Electrochemical characterization of the assembled half-batteries: cyclic voltammetry curves at  $0.1 \text{ mV s}^{-1}$  within 0.01–1.5 V vs.  $\text{Li}/\text{Li}^+$  for (a) unmodified and (b) Sr-modified anodes, and Nyquist plots for (c) the uncycled anode and (d) anode after 5 cycles. The data are marked by points for experiment and by line for fitting results according to the equivalent circuit diagram inserted.

Table 2  $R_{ct}$  values obtained by fitting Nyquist diagrams *via* the given equivalent circuit

Sample	$R_{ct}$ for uncycled anode ( $\Omega$ )	$R_{ct}$ for anode after 5 cycles ( $\Omega$ )
Unmodified	97.0	100.0
Sr-modified	79.8	68.4



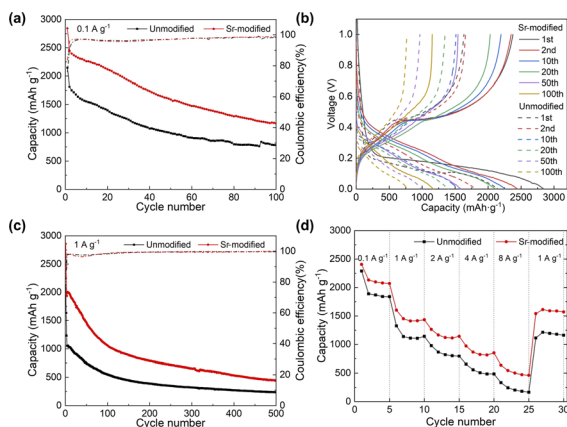


Fig. 5 Performance of the as-assembled half-batteries: (a) cycle performance at  $0.1 \text{ A g}^{-1}$  from 0.1 to 1 V, (b) voltage profiles for the 1st, 2nd, 10th, 20th, 50th, and 100th cycle, (c) cycle performance at  $1 \text{ A g}^{-1}$ , and (d) capability at the current densities of 0.1, 1, 2, 4 and  $8 \text{ A g}^{-1}$ .

the special architecture is favoured for the lithium insertion and removal. Fig. 5(c) gives the cycle performance at  $1 \text{ A g}^{-1}$ . After 100 cycles, the unmodified anode delivers a capacity of  $548.9 \text{ mA h g}^{-1}$  and that decreases to  $237.4 \text{ mA h g}^{-1}$  after 500 cycles. However, the modified one remains  $1058.7 \text{ mA h g}^{-1}$  and  $445 \text{ mA h g}^{-1}$ , respectively. In addition, as presented in Fig. 5(d), the unmodified electrode delivers average capacities of 1945.2, 1163.7, 850.7, 537.9, 224.4 and  $1171.4 \text{ mA h g}^{-1}$ , at current densities of 0.1, 1, 2, 4, 8 and  $1 \text{ A g}^{-1}$ , respectively. However, with the same set, the Sr-modified electrode has much higher capabilities of 2156.2, 1461.7, 1160.3, 863.8, 523.3 and  $1579.5 \text{ mA h g}^{-1}$ . The excellent rate performance of the Sr-modified electrode is dominated by the stability of SiGe structure, owing to the rich fibrous branches as well as the favourable porosity.

Fig. 6 presents the morphologies of the unmodified and Sr-modified SiGe anodes before and after 100 charge/discharge cycles. Compared to the unmodified anode, the Sr-modified

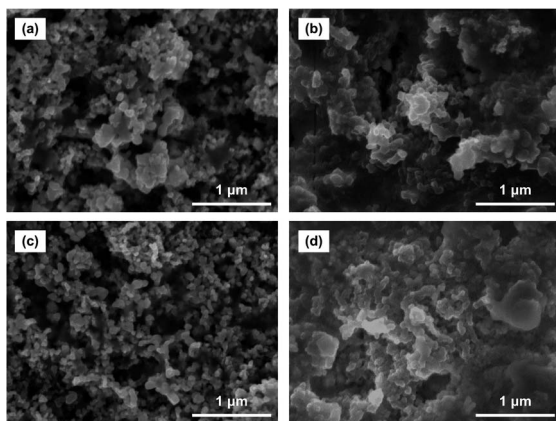


Fig. 6 SEM morphological images of the (a and b) unmodified and (c and d) Sr-modified SiGe anodes (a and c) before and (b and d) after 100 charge/discharge cycles, respectively.

anode shows a more uniform and consistent structure before cycling, which enhances the structure stability during the following charge and discharge process. After 100 cycles, the unmodified anode appears some sharp cracks while the Sr-modified one remains the structure integrity basically. Therefore, the Sr-modified SiGe anode exhibits dramatically enhanced electrochemical performance with outstanding stability and superior rate capability. The modification strategy makes it possible for SiGe anodes to serve in more demanding conditions, especially those fields urgently requiring longer life and faster charge/discharge.

### Comparison and evaluation

To evaluate the excellent electrochemical performance of as-prepared SiGe particles, we compared our experimental results with the work of Yang *et al.*<sup>8</sup> in the literature. The data used for comparison were extracted from the original figures in the literature *via* the software GETDATA. As presented in Fig. 7, Yang *et al.*<sup>8</sup> adjusted the Al content in the precursor to control the morphology and porosity, and found that when the precursor contains 80% Al, the  $\text{Si}_{12}\text{Ge}_8$  anode presents the best reversible capacity with an average value of  $503.2 \text{ mA h g}^{-1}$  at the current density of  $8 \text{ A g}^{-1}$ . Under the same condition for measurement, our SiGe electrodes dealloyed from the Sr-modified precursor perform a superior capacity of  $675.3 \text{ mA h g}^{-1}$ , which is much higher than the aforementioned anodes. Besides, as listed in Table 3, within the whole current range for the measurement of rate capability, our dealloyed SiGe electrodes deliver higher capacities than the electrochemical deposited ones, no matter the axial Si(Ge) homogeneous and heterostructure nanowires.<sup>17,43,44</sup> Also, compared the Sr-modified pure Si anodes,<sup>28</sup> the alloying strategy of Ge improves not only the cycle performance but also the rate capability. Overall, SiGe particles dealloyed from Sr-modified Al-Si-Ge eutectic precursor are comparable to previous work about facile synthesis of Si and SiGe anodes without post-treatment, no matter the synthesis methods. Our strategy is based on the idea that Sr is a kind of modification elements for eutectic Al-Si(Ge) alloys and it can indeed modify the electrochemical performance. In fact, there are also other modification elements for hypereutectic Al-Si alloys such as P, which are also

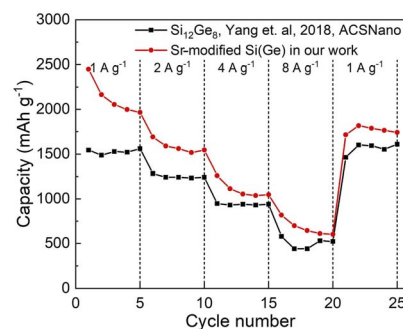


Fig. 7 Capability of batteries in this work at the current densities of 0.1, 1, 2, 4 and  $8 \text{ A g}^{-1}$ , compared with the work of Yang *et al.*<sup>8</sup>



Table 3 Electrochemical performance of some representative Si-based anodes in literature

Electrodes	Cycle performance	Rate capability
Sr-modified SiGe in this work	1318.1 mA h g <sup>-1</sup> at 0.1 A g <sup>-1</sup> after 80 cycles 847.1 mA h g <sup>-1</sup> at 1 A g <sup>-1</sup> after 80 cycles	1102.52 mA h g <sup>-1</sup> at 4 A g <sup>-1</sup> 675.3 mA h g <sup>-1</sup> at 8 A g <sup>-1</sup>
SiGe dealloyed from Al <sub>80</sub> Si <sub>12</sub> Ge <sub>8</sub> <sup>8</sup>	1364 mA h g <sup>-1</sup> at 0.1 A g <sup>-1</sup> after 80 cycles	938 mA h g <sup>-1</sup> at 4 A g <sup>-1</sup>
SiGe dealloyed from Al <sub>85</sub> Si <sub>9</sub> Ge <sub>6</sub> <sup>8</sup>	1072 mA h g <sup>-1</sup> at 0.1 A g <sup>-1</sup> after 80 cycles	503.2 mA h g <sup>-1</sup> at 8 A g <sup>-1</sup>
Si <sub>0.67</sub> Ge <sub>0.33</sub> <sup>17</sup>	1395 mA h g <sup>-1</sup> at 0.2C after 100 cycles	607 mA h g <sup>-1</sup> at 5C 317 mA h g <sup>-1</sup> at 10C
Si <sub>0.50</sub> Ge <sub>0.50</sub> <sup>17</sup>	1265 mA h g <sup>-1</sup> at 0.2C after 100 cycles	657 mA h g <sup>-1</sup> at 5C 357 mA h g <sup>-1</sup> at 10C
Si dealloyed from Al <sub>77.8</sub> Si <sub>12.2</sub> <sup>33</sup>	595 mA h g <sup>-1</sup> at 2 A g <sup>-1</sup> after 50 cycles	235.4 mA h g <sup>-1</sup> at 2 A g <sup>-1</sup>
SiGe <sup>43</sup>	1389 mA h g <sup>-1</sup> at 0.2C after 100 cycles	959.6 mA h g <sup>-1</sup> at 5C 620.6 mA h g <sup>-1</sup> at 10C
Si <sup>44</sup>	1772 mA h g <sup>-1</sup> at 0.2C after 30 cycles	312.6 mA h g <sup>-1</sup> at 5C 69 mA h g <sup>-1</sup> at 10C
SiGe <sup>44</sup>	1259 mA h g <sup>-1</sup> at 0.2C after 30 cycles	425.6 mA h g <sup>-1</sup> at 5C 66 mA h g <sup>-1</sup> at 10C
Ge <sup>44</sup>	776 mA h g <sup>-1</sup> at 0.2C after 30 cycles	289 mA h g <sup>-1</sup> at 5C 156 mA h g <sup>-1</sup> at 10C

promising to improve the performance of SiGe-based anodes and are worth exploring. What's more, the posttreatments that have been explored by researchers can also be applied to further improve the performance, such as the pre-lithiation, surface coating, advanced binders, and so on.

## Conclusions

In summary, by adding minor Sr to the Al<sub>84.23</sub>Si<sub>9.46</sub>Ge<sub>6.31</sub> eutectic alloy, the eutectic SiGe in the arc-melted castings as well as melt-spun ribbons transits from flake to fibrous morphology. The SiGe particles dealloyed from the ribbon precursors have porous coral-like nano-architectures. However, the Sr-modified SiGe particles have more fibrous branches towards various directions, contributing the anode with a larger surface area and porosity, correspondingly more active reaction positions and larger space to accommodate the volume change during the lithiation/de-lithiation process. Therefore, the electrochemical performance of the as-synthesized SiGe particles is improved significantly.

Sr-modified SiGe anode performs a great ICE of 83.62% and remains 1166.6 mA h g<sup>-1</sup> at 0.1 A g<sup>-1</sup> after 100 cycles. Also, The Sr-modified SiGe anodes perform a superior reversible rate capacity of 675.3 mA h g<sup>-1</sup> at the current density of 8 A g<sup>-1</sup>, which is much higher than that reported in previous studies. What's more, this work introduces the modification in metallurgy into the synthesis of battery electrodes and other energy storage materials, and gives an effective strategy to improve the performance and accelerate their industrial applications.

## Author contributions

Huajie Zhang: investigation; methodology; data curation; formal analysis; writing – original draft, Jinfu Li: conceptualization; validation; funding acquisition; project administration; supervision; writing – review & editing.

## Conflicts of interest

There are no conflicts to declare.

## Acknowledgements

This work was supported by the National Natural Science Foundation of China (Grant Nos. 51620105012 and 51821001).

## Notes and references

- J. M. Tarascon and M. Armand, Issues and challenges facing rechargeable lithium batteries, *Nature*, 2001, **414**, 359–367.
- N. Nitta, F. Wu, J. T. Lee and G. Yushin, Li-ion battery materials: present and future, *Mater. Today*, 2015, **18**, 252–264.
- W. Tao, P. Wang, Y. You, K. Park, C. Wang, Y. Li, F. Cao and S. Xin, Strategies for improving the storage performance of silicon-based anodes in lithium-ion batteries, *Nano Res.*, 2019, **12**, 1739–1749.
- D. Ma, Z. Cao and A. Hu, Si-Based anode materials for Li-ion batteries: a mini review, *Nano-Micro Lett.*, 2014, **6**, 347–358.
- C. Zhu, K. Han, D. Geng, H. Ye and X. Meng, Achieving high-performance silicon anodes of lithium-ion batteries via atomic and molecular layer deposited surface coatings: an overview, *Electrochim. Acta*, 2017, **251**, 710–728.
- E. Pollak, G. Salitra, V. Baranchugov and D. Aurbach, *In situ* conductivity, impedance spectroscopy, and *ex situ* Raman spectra of amorphous silicon during the insertion/extraction of lithium, *Phys. Chem.*, 2007, **111**, 11437–11444.
- X. Su, Q. Wu, J. Li, X. Xiao, A. Lott, W. Lu, B. W. Sheldon and J. Wu, Silicon-based nanomaterials for lithium-ion batteries: a review, *Adv. Energy Mater.*, 2014, **4**, 1300882.
- Y. Yang, S. Liu, X. Bian, J. Feng, Y. An and C. Yuan, Morphology- and porosity- tunable synthesis of 3D nanoporous SiGe alloy as a high-performance lithium-ion battery anode, *ACS Nano*, 2018, **12**, 2900–2908.



- 9 B. Zhu, G. Liu, G. Lv, Y. Mu, Y. Zhao, Y. Wang, X. Li, P. Yao, Y. Deng, Y. Cui and J. Zhu, Minimized lithium trapping by isovalent isomorphism for high initial coulombic efficiency of silicon anodes, *Sci. Adv.*, 2019, **5**, 2375–2548.
- 10 N. Lin, L. Wang, J. Zhou, J. Zhou, Y. Han, Y. Zhu, Y. Qian and C. Cao, A Si/Ge nanocomposite prepared by a one-step solid-state metathesis reaction and its enhanced electrochemical performance, *J. Mater. Chem. A*, 2015, **3**, 11199–11202.
- 11 Y. Zhang, N. Du, C. Xiao, S. Wu, Y. Chen, Y. Lin, J. Jiang, Y. He and D. Yang, Simple synthesis of SiGe@C porous microparticles as high-rate anode materials for lithium-ion batteries, *RSC Adv.*, 2017, **7**, 33837–33842.
- 12 L. Sun, J. Xie and Z. Jin, Different dimensional nanostructured silicon materials: from synthesis methodology to application in high-energy lithium-ion batteries, *Energy Technol.*, 2019, **7**, 1900962.
- 13 M. Ge, X. Fang, J. Rong and C. Zhou, Review of porous silicon preparation and its application for lithium-ion battery anodes, *Nanotechnol.*, 2013, **24**, 422001.
- 14 X. Zuo, J. Zhu, P. Müller-Buschbaum and Y. Cheng, Silicon based lithium-ion battery anodes: a chronicle perspective review, *Nano Energy*, 2017, **31**, 113–143.
- 15 R. Ma, Y. Liu, Y. Yang, M. Gao and H. Pan, Mg<sub>2</sub>Si anode for Li-ion batteries: Linking structural change to fast capacity fading, *Appl. Phys. Lett.*, 2014, **105**, 213901.
- 16 R. Venkatesan, M. K. Arivalagan, V. Venkatachalapathy, J. M. Pearce and J. Mayandi, Effects of silver catalyst concentration in metal assisted chemical etching of silicon, *Mater. Lett.*, 2018, **221**, 206–210.
- 17 K. Stokes, H. Geaney, G. Flynn, M. Sheehan, T. Kennedy and K. M. Ryan, Direct synthesis of alloyed Si<sub>1-x</sub>Ge<sub>x</sub> nanowires for performance-tunable lithium-ion battery anodes, *ACS Nano*, 2017, **11**, 10088–10096.
- 18 P. Liu, J. Zheng, Y. Qiao, H. Li, J. Wang and M. Wu, Fabrication and characterization of porous Si–Al films anode with different macroporous substrates for lithium-ion batteries, *J. Solid State Electrochem.*, 2014, **18**, 1799–1806.
- 19 P. R. Abel, A. M. Chockla, Y. M. Lin, V. C. Holmberg, J. T. Harris, B. A. Korgel, A. Heller and C. B. Mullins, Nanostructured Si<sub>(1-x)</sub>Ge<sub>x</sub> for tunable thin film lithium-ion battery anodes, *ACS Nano*, 2013, **7**, 2249–2257.
- 20 Z. Jiang, C. Li, S. Hao, S. Hao, K. Zhu and P. Zhang, An easy way for preparing high-performance porous silicon powder by acid etching Al–Si alloy powder for lithium-ion battery, *Electrochim. Acta*, 2014, **115**, 393–398.
- 21 T. Jiang, R. Zhang, Q. Yin, W. Zhou, Z. Dong, N. A. Chernova, Q. Wang, F. Omenya and M. S. Whittingham, Morphology, composition and electrochemistry of a nanoporous silicon versus bulk silicon anode for lithium-ion batteries, *J. Mater. Sci.*, 2016, **52**, 3670–3677.
- 22 L. Lu, Nanoporous noble metal-based alloys: a review on synthesis and applications to electrocatalysis and electrochemical sensing, *Mikrochim. Acta*, 2019, **186**, 664.
- 23 Y. An, Y. Tian, C. Wei, Y. Tao, B. Xi, S. Xiong, J. Feng and Y. Qian, Dealloying: an effective method for scalable fabrication of 0D, 1D, 2D, 3D materials and its application in energy storage, *Nano Today*, 2021, **37**, 101094.
- 24 M. Sohn, D. G. Lee, H.-I. Park, C. Park, J. H. Choi and H. Kim, Microstructure controlled porous silicon particles as a high capacity lithium storage material via dual step pore engineering, *Adv. Funct. Mater.*, 2018, **28**, 1800855.
- 25 F. Zu and X. Li, Functions and mechanism of modification elements in eutectic solidification of Al–Si alloys: a brief review, *China Foundry*, 2014, **11**, 287–309.
- 26 K. Nogita, H. Yasuda, M. Yoshiya, S. D. McDonald, K. Uesugi, A. Takeuchi and Y. Suzuki, The role of trace element segregation in the eutectic modification of hypoeutectic Al–Si alloys, *J. Alloys Compd.*, 2010, **489**, 415–420.
- 27 Q. Liu, M. Liu, C. Xu, W. Xiao, H. Yamagata, S. Xie and C. Ma, Effects of Sr, Ce and P on the microstructure and mechanical properties of rapidly solidified Al–7Si alloys, *Mater. Charact.*, 2018, **140**, 290–298.
- 28 P. Jiang and J. Li, A porous silicon anode prepared by dealloying a Sr-modified Al–Si eutectic alloy for lithium-ion batteries, *RSC Adv.*, 2022, **12**, 7892–7897.
- 29 H. Jones, The status of rapid solidification of alloys in research and application, *J. Mater. Sci.*, 1984, **19**, 1043–1076.
- 30 F. Alshmiri, Rapid solidification processing: melt spinning of Al-high Si alloys, *Adv. Mater. Res.*, 2012, **383–390**, 1740–1746.
- 31 J. L. Murray and A. J. McAlister, The Al–Si (aluminum–silicon) system, *Bull. Alloy Phase Diagrams*, 1984, **5**, 74–84.
- 32 H. Okamoto, Al–Ge (aluminum–germanium), *J. Phase Equilib. Diffus.*, 1998, **19**, 86.
- 33 I. N. Ganiev and L. V. Zheleznyak, Construction of the liquidus surface for the Al–Si–Ge system by the simplex experiment planning method, *Russ. Metall.*, 1983, **4**, 146–149.
- 34 M. D. Giovanni, J. A. Kaduk and P. Srirangam, Modification of Al–Si alloys by Ce or Ce with Sr, *JOM*, 2018, **71**, 426–434.
- 35 S. Shankar, Y. W. Riddle and M. M. Makhlof, Eutectic Solidification of Aluminum–Silicon Alloys, *Metall. Mater. Trans. A*, 2004, **35**, 3038–3043.
- 36 S. NatureHegde and K. N. Prabhu, Modification of eutectic silicon in Al–Si alloys, *J. Mater. Sci.*, 2008, **43**, 3009–3027.
- 37 A. Hellawell, The growth and structure of eutectics with silicon and germanium, *Prog.*, 1970, **15**, 3–78.
- 38 S. Z. Lu and A. Hellawell, The mechanism of silicon modification in aluminum-silicon alloys: Impurity induced twinning, *Metall. Mater. Trans. A*, 1987, **18**, 1721–1733.
- 39 H. Li, F. Yue, C. Yang, P. Xue, N. Li, Y. Zhang and J. Wang, Structural evolution of a metal–organic framework and derived hybrids composed of metallic cobalt and copper encapsulated in nitrogen-doped porous carbon cubes with high catalytic performance, *CrystEngComm*, 2017, **19**, 64–71.
- 40 P. Schneider, Adsorption isotherms of microporous–mesoporous solids revisited, *Appl. Catal., A*, 1995, **129**, 157–165.
- 41 J. Yu, N. Du, J. Wang, H. Zhang and D. Yang, SiGe porous nanorod arrays as high-performance anode materials for lithium-ion batteries, *J. Alloys Compd.*, 2013, **577**, 564–568.
- 42 J. Feng, Z. Zhang, L. Ci, W. Zhai, Q. Ai and S. Xiong, Chemical dealloying synthesis of porous silicon anchored by *in situ* generated graphene sheets as anode material for lithium-ion batteries, *J. Power Sources*, 2015, **287**, 177–183.



## Paper

- 43 K. Stokes, G. Flynn, H. Geaney, G. Bree and K. M. Ryan, Axial Si–Ge heterostructure nanowires as lithium-ion battery anodes, *Nano Lett.*, 2018, **18**, 5569–5575.
- 44 S. Kilian, K. McCarthy, K. Stokes, T. E. Adegoke, M. Conroy, I. S. Amiin, H. Geaney, T. Kennedy and K. M. Ryan, Direct

growth of Si, Ge, and Si–Ge heterostructure nanowires using electroplated Zn: an inexpensive seeding technique for Li-ion alloying anodes, *Small*, 2021, **17**, 2005443.

